Adaptive partitioning for 3D Gabor wavefield extrapolation

Yongwang Ma and Gary F. Margrave

ABSTRACT

Adaptive partitioning algorithms in 1D have been developed and applied to improve the 2D Gabor imaging efficiency. These algorithms reduce the computation redundancy in Gabor imaging without sacrificing accuracy. A new adaptive partitioning algorithm in 1D using lateral position error as the criterion is described in another paper in this volume. In this paper, we extend the adaptive partitioning technique to 2D as required for 3D Gabor depth imaging. Some tests of the 2D adaptive partitioning are presented to show that the algorithm works properly 2D horizontal slices of 3D velocity models. We also present some results of 3D impulse response tests using the Gabor extrapolator.

INTRODUCTION

Gabor wavefield extrapolation can be used to approximate the generalized phase shift plus interpolation (GPSPI) (Margrave and Ferguson, 1999; Margrave et al., 2004, 2006) and the non-stationary phase shift (NSPS) methods (Ferguson and Margrave, 2002). Gabor imaging is easily formulated using a conventional Gabor transform which employs narrow localizing windows at all locations. This is unnecessary when the lateral velocity variation is very small. In these cases, we may use fewer wider localizing windows (or partitions) instead of many narrow ones, resulting in lower computational effort without sacrificing accuracy. The challenge is to find the optimal window width as dictated by the lateral velocity variation. With such adaptive partitioning algorithms, we are able to control the trade-off between computation speed and imaging accuracy.

We have investigated three criteria for adaptive partitioning. The first one was described by Grossman et al. (2002); this method used the lateral velocity gradient to control the number of windows (partitions). The threshold was set proportional to the relative velocity variation along the lateral coordinate. This works very well in the Gabor depth imaging on the Marmousi dataset (e.g. Ma and Margrave, 2005b). However, some tests showed that this method is direction-dependent; i.e., when doing adaptive partitioning in an opposite direction, one can get a different set of partitions. Also, the threshold is somewhat arbitrary, having no direct link with imaging accuracy, and must be set by intuition.

In the second adaptive partition algorithm, Partitions are generated according to the phase error between the GPSPI extrapolator and the Gabor extrapolator (an approximation to the former one) (Ma and Margrave, 2005a). The algorithm has been applied in Gabor depth imaging, and good imaging results were also presented (Ma and Margrave, 2006b). Also, it is not obvious how to extend either of these first two methods to the 2D partitioning required for 3D imaging.

The third criterion is called adaptive partitioning using an estimation of lateral position error. Lateral position error is implicitly related to the phase error; however, it is easier to implement in 2D (or higher dimensions).

In the following sections, we will demonstrate how to extend the adaptive partitioning with lateral position error criterion from 1D to 2D.

METHOD

Approximation of GPSPI in 3D

The Gabor extrapolator has been developed as an approximation of the GPSPI extrapolator. GPSPI extrapolation is an "locally homogeneous" wavefield extrapolation method; 3D extrapolation with GPSPI can be explicitly written as (after Margrave and Ferguson, 1999; Margrave et al., 2004)

$$\begin{aligned}\psi\left(x,y,\Delta z,\omega\right) &= \frac{1}{4\pi^2}\int_{\mathbb{R}^2}\hat{\psi}\left(k_x,k_y,0,\omega\right)\hat{W}\left(k(x,y),k_x,k_y,\Delta z\right)\\ &\quad\cdot\exp\left(-i(k_x x+k_y y)\right)\mathrm{d}k_x\mathrm{d}k_y,\end{aligned}\tag{1}$$

where

$$k(x,y)=\frac{\omega}{v(x,y)},\tag{2}$$

x and y denote the transverse coordinates, k_x and k_y are the transverse wavenumbers, k_x, k_y and k_z (to be defined in the following) compose the total wavenumber vector whose magnitude is k, Δz is the extrapolation step size, ω is temporal angular frequency, and $v(x,y)$ is the velocity, which is allowed to vary only laterally within a single depth step. Equation (1) extrapolates wavefields from depth 0 down to depth Δz in the frequency-wavenumber domain and transforms them into the frequency-space domain using a generalized inverse Fourier transform. $\hat{\psi}\left(k_x,k_y,0,\omega\right)$ is the Fourier spectrum of $\psi\left(x,y,0,t\right)$ (seismic data recorded on the surface) defined as

$$\hat{\psi}\left(k_x,k_y,0,\omega\right)=\int_{\mathbb{R}^3}\psi\left(x,y,0,t\right)\exp\left(i(k_x x+k_y y-\omega t)\right)\mathrm{d}x\mathrm{d}y\mathrm{d}t.\tag{3}$$

Equations (1) and (3) indicate the convention for the forward and inverse Fourier transforms in this paper. $\hat{W}$ in (1) is called the GPSPI wavefield extrapolator, defined as the spatial phase shift operator

$$\hat{W}\left(k(x,y),k_x,k_y,\Delta z\right)=\exp\left(ik_z\left(k(x,y),k_x,k_y\right)\Delta z\right)\tag{4}$$

and

$$k_z\left(k(x,y),k_x,k_y\right)=\begin{cases}\sqrt{k^2(x,y)-(k_x^2+k_y^2)}, & k^2(x,y)>k_x^2+k_y^2\\ i\sqrt{(k_x^2+k_y^2)-k^2(x,y)}, & k^2(x,y)<k_x^2+k_y^2.\end{cases} \tag{5}$$

The development of the Gabor approximation to the GPSPI extrapolator is very similar to the one shown in another paper in this volume (refer to Ma and Margrave, 2006a); i.e.,

$$\hat{W}\left(k(x,y),k_x,k_y,\Delta z\right)\approx\sum_{j\in\mathbb{Z}}\Omega_j(x,y)S_j(x,y)\hat{W}\left(k_j,k_x,k_y,\Delta z\right), \tag{6}$$

where

$$k_j=\frac{\omega}{v_j} \tag{7}$$

and Ω_j is a set of 2D windows forming a partition of unity (POU) in 2D, which means

$$\sum_{j\in\mathbb{Z}}\Omega_j(x,y)=1, \tag{8}$$

where $\mathbb{Z}$ is the integer set. The split-step Fourier operator (Stoffa et al., 1990), dealing with phase residual due to small velocity fluctuations, is written as

$$S_j(x,y)=\exp\left(i\omega\Delta z\left(\frac{1}{v(x,y)}-\frac{1}{v_j}\right)\right), \tag{9}$$

and $\hat{W}\left(k_j,k_x,k_y,\Delta z\right)$ is a wavefield extrapolator related to reference velocities v_j defined as

$$v_j=\frac{\int_{\mathbb{R}^2}\Omega_j(x,y)v(x,y)\mathrm{d}x\mathrm{d}y}{\int_{\mathbb{R}^2}\Omega_j(x,y)\mathrm{d}x\mathrm{d}y}. \tag{10}$$

Using Gabor approximation ψ_G, GPSPI formula (1) can be written as

$$\psi(x,y,\Delta z,\omega)\approx\psi_G(x,y,\Delta z,\omega) \tag{11}$$

and

$$\begin{aligned}\psi_G(x,y,\Delta z,\omega) &= \sum_{j\in\mathbb{Z}}\Omega_j(x,y)S_j(x,y)\int_{\mathbb{R}^2}\hat{\psi}(k_x,k_y,0,\omega)\hat{W}\left(k_j,k_x,k_y,\Delta z\right)\\ &\quad\cdot\exp\left(-i(k_xx+k_yy)\right)\mathrm{d}k_x\mathrm{d}k_y,\end{aligned} \tag{12}$$

where $\Omega_j(x,y)$ and $S_j(x,y)$ are (k_x,k_y) independent and taken out of the integrand.

Building Adaptive Partitions for 3D Gabor Imaging

The creation of partitions $\Omega_j(x,y)$ is the key to efficient 3D Gabor depth imaging. The steps to build the adaptive partitions in 2D using the lateral position error criterion are very similar to the ones we described in 1D (refer to Ma and Margrave, 2006a).

Beginning with a local ray path at point O (see Figure 1), we have the geometry relationship in the spatial domain as

$$\rho = \Delta z \tan\theta, \tag{13}$$

where $\rho = \sqrt{x^2+y^2}$ is the lateral distance in the plane of $z=0$; θ is the scattering angle (between the vertical direction and the ray path) of the ray. Similarly, in the wavenumber domain, we have

$$k = \frac{k_\rho}{\sin\theta} = \frac{\omega}{v(x,y)} \tag{14}$$

and

$$k_\rho = \sqrt{k_x^2+k_y^2}. \tag{15}$$

Differentiating on both sides of equations (14) and (15) gives

$$\delta\rho = \Delta z \sec^2\theta \frac{\partial\theta}{\partial v}\delta v \tag{16}$$

and

$$\frac{\partial\theta}{\partial v} = \frac{k_\rho}{\omega}\sec\theta. \tag{17}$$

Equations (16) and (17) gives

$$\delta v = \frac{\cos^3\theta}{\sin\theta}\frac{\delta\rho}{\Delta z}v. \tag{18}$$

Equation (18) is the formula to calculate the velocity fluctuation δv given a velocity v, the lateral position error $\delta\rho$, extrapolation step size Δz and the scattering angle θ. This formula determines the reference velocities for Gabor wavefield extrapolation given those

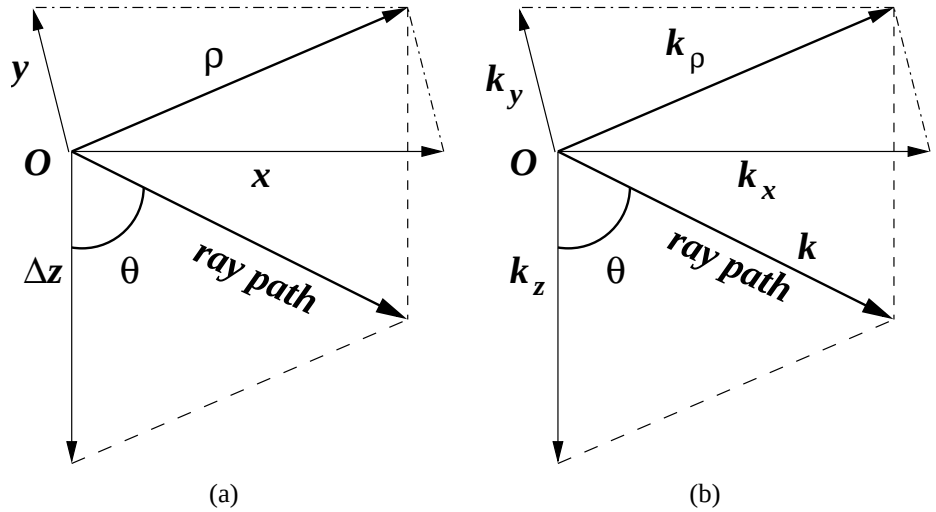

FIG. 1. Geometrical relationships of a local ray between the vertical and lateral components in the spatial (a) and wavenumber (b) domains.

parameters. If we fix the scattering angle θ, such as the maximum scattering angle, and Δz, lateral position error $\delta\rho$ can be used as the criterion to define the reference velocities. Lateral position error is related to the accuracy of approximation, the image quality.

To specify the reference velocities, v_1 is chosen as the most frequently occurring velocity (easily chosen from a histogram of the discretely sampled $v(x, y)$) and then δv_1 is obtained from equation (18) as $\delta v_1 = a v_1$, where $a = \left(\cos^3\theta \sin^{-1}\theta \delta\rho/\Delta z\right)$. Letting v_2 denote the next higher reference velocity and v_3 the next lower, the conditions

$$v_1 - \frac{1}{2}\delta v_1 = v_3 + \frac{1}{2}\delta v_3 = v_3(1 + \frac{1}{2}a) \tag{19}$$

and

$$v_1 + \frac{1}{2}\delta v_1 = v_2 - \frac{1}{2}\delta v_2 = v_2(1 - \frac{1}{2}a) \tag{20}$$

allow calculation of v_2 and v_3 as

$$v_2 = \frac{2v_1 + \delta v_1}{2 - a} \tag{21}$$

and

$$v_3 = \frac{2v_1 - \delta v_1}{2 + a}. \tag{22}$$

Proceeding in a similar fashion until reference velocities exceeding the range of $v(x, y)$ are found defines a complete set of reference velocities. The use of equation (18) in selecting distance between reference velocities suggests that the lateral position error will be bounded by $\delta\rho$. This bound may not be strictly held because equation (18) was derived constant velocity theory; however, it should still be a useful constraint.

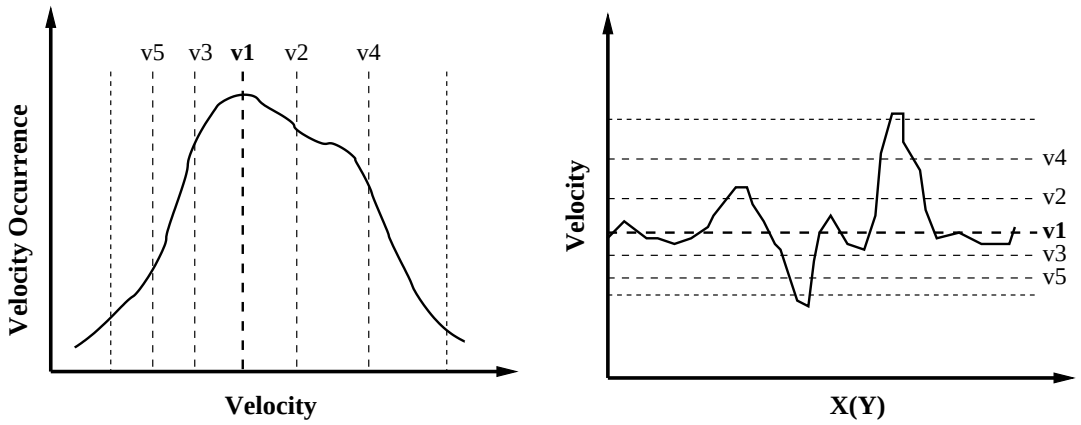

FIG. 2. Determine the reference velocities and build indication functions. (a) v_1 is chosen as the most frequently occurring velocity and the other reference velocities are chosen at spacings determined by the position error criterion. (b) The j^{th} indicator function is unity at those locations where v_j is the closest reference velocity to $v(x, y)$ and are zeros elsewhere.

Once all the reference velocities are known, they can be used as measures (see Figure 2 (b)) to create the indicator function $I_j(x, y)$,

$$I_j\,(x,y) = \begin{cases} 1, & |v(x,y) - v_j\,| = \min \\ \\ 0, & \text{otherwise}, \end{cases} \tag{23}$$

where $v(x, y)$ is the exact velocity at lateral position (x, y), $v_j\,(j = 1, 2, ..., n)$ are reference velocities calculated using equation (18). Each of these reference velocities is used as a plane of certain 'altitude' to calibrate velocity values across the layer (plane). The positions with the closest velocity values to this reference velocity will be assigned "1's", otherwise, "0's" in the corresponding indicator function.

By construction, the indicator functions form a POU however they vary discontinuously with position. A normalized convolution of each indicator function $I_j(x, y)$ with a 2D atomic window (see Figure 3) creates smoothly continuous partitions (forming a POU). These partitions correspond to reference velocities in the Gabor wavefield extrapolation. This is done by

$$\Omega_j(x, y) = (I_j * \Theta)\,(x, y), \tag{24}$$

where Θ is the atomic window. The atomic window can be any type of bump function, such as the Gaussian window, whose width is roughly equal to the grid spacing; $*$ is a symbol

of the normalized convolution. The normalization is chosen such that the Ω_j also form a POU and amounts to division by the sum of the samples of the bump function.

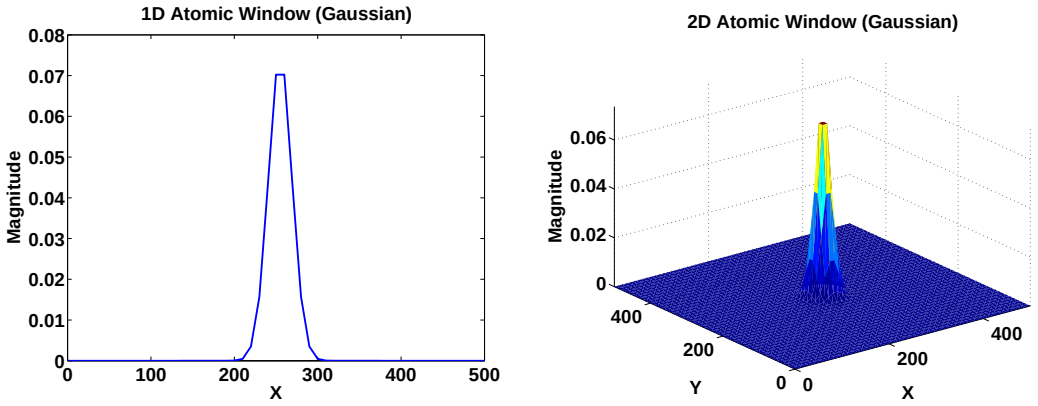

(a) (b)

FIG. 3. Atomic Windows. (a) 1D atomic window. (b) 2D atomic window.

In the next section, some examples of the adaptive partitioning using the lateral position error criterion are shown.

ADAPTIVE PARTITIONING EXAMPLES

The first partitioning example is a pseudo-2D velocity model, which means that in the y direction there are no velocity variations; in the x direction there is a velocity bump (higher velocity) in the middle part (see Figure 4 (a) in red colour). A 2.5 meter lateral position error is used in this and the following partitioning examples.

Similar to the bump example in 1D, we have two partitions for the bump velocity model in 2D. The first partition is related to the lower velocity zones (in blue) on both sides in the bump velocity model (see Figure 4 (a) and (b)); the second partition corresponds to the 'bump' (high velocity zone, in red). Figure 4 (d) shows the summation of the two partitions to obtain unity.

The second velocity model contains a few velocity chunks confined by polygons. The velocity model and the resulting partitions are shown in Figure 5 (a) and (b)-(g), respectively. There are two chunks (two triangles in the upper left and lower left corners in dark blue) with the same velocity values and hence correspond to the same window. The rest of the chunks have different velocity values from each other. As predicted, the two triangular zones will share a single partition (see Figure 5 (b)); the rest of the areas have their own partitions (see Figure 5 (c)-(g)). Comparing velocity chunks in Figure 5 (a) and those partitions generated by the 2D partitioning algorithm, we know that they match exactly.

Those 'gaps' in Figure 5 (h) are related to the boundaries of the velocity chunks (compare Figure 5 (a) to (h)). It shows that we have good matches between the velocity chunks and the partitions generated by the 2D adaptive partitioning algorithm. These 2D partitions also form a POU (see Figure 5 (i)).

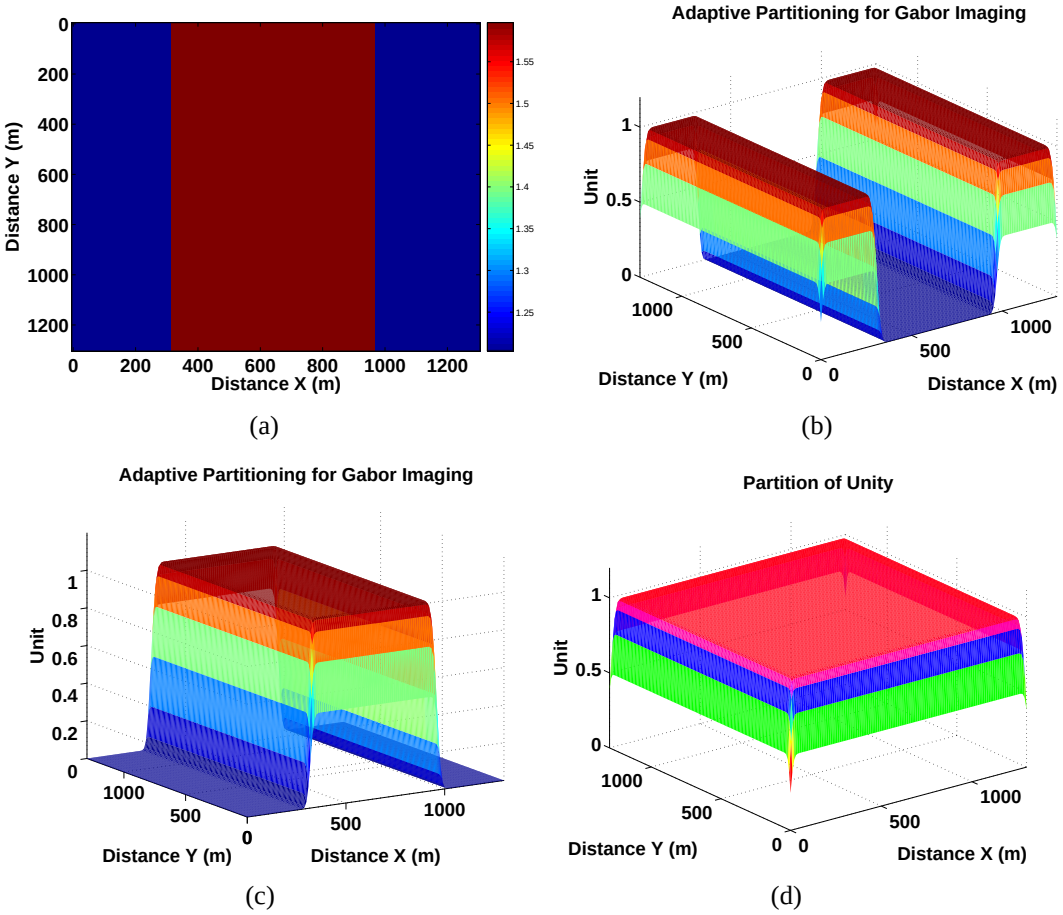

FIG. 4. Adaptive partitioning on a bump velocity model. (a) Velocity model. (b) The first partition: related to the low velocity zones in blue in (a). (c) The second partition: related to the high velocity bump in the middle red part in (a). (d) POU (summation of the partitions in (b) and (c).

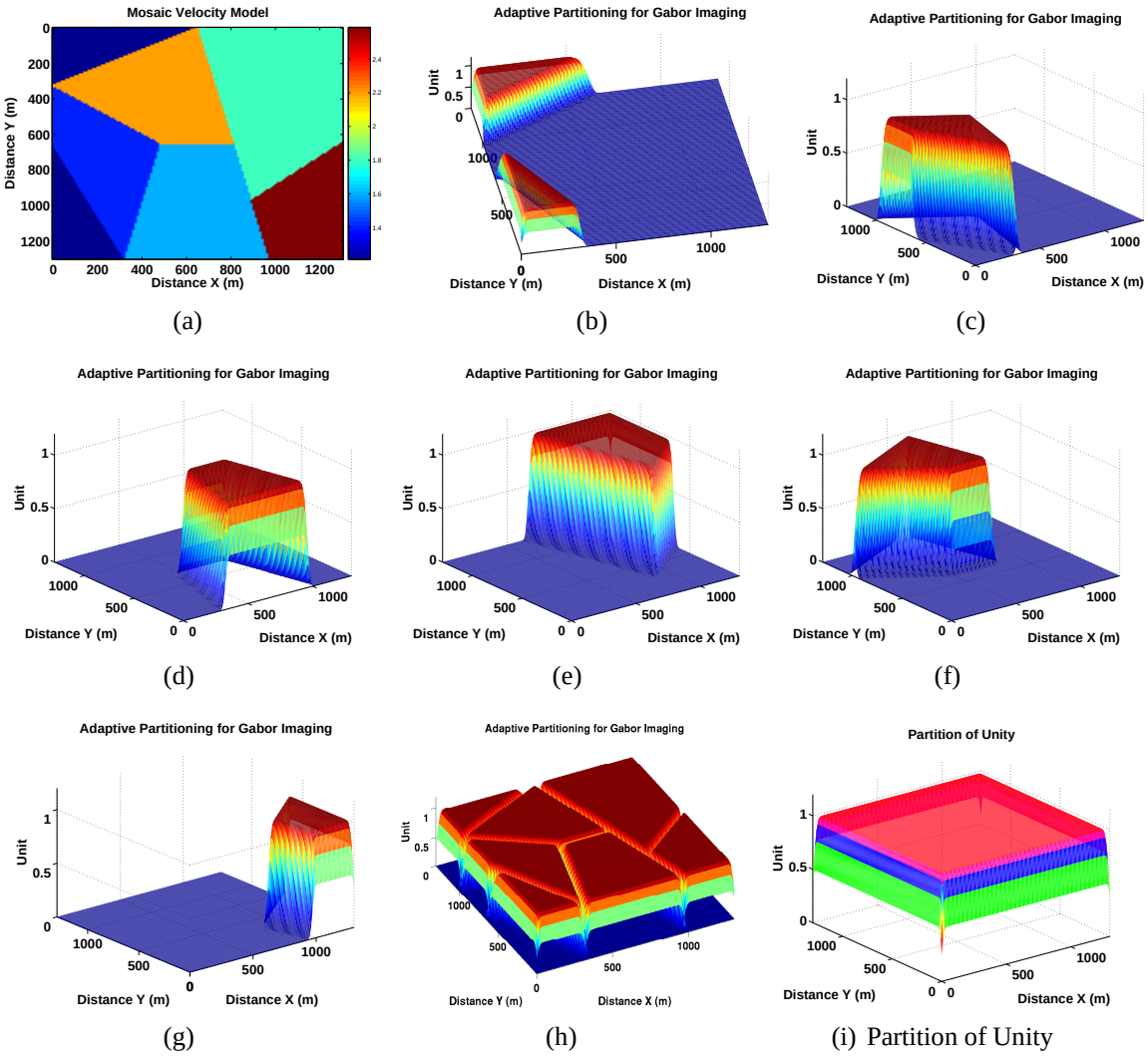

FIG. 5. Adaptive partitioning on the mosaic velocity model. (a) Velocity model. (b) The first partition: triangles in dark blue in (a). (c) The second partition: area in sky blue adjacent to the lower triangle in (a). (d) The third partition: area in light blue at the bottom of (a). (e) The fourth partition: area in light green in the upper right corner of (a). (f) The fifth partition: area in yellow in (a). (g) The sixth partition: area in red in (a). (h) All the partitions. (i) Partition of Unity.

Building adaptive partitions in the 2D velocity models is one of the key steps to implement adaptive Gabor imaging in 3D. Through the partitioning examples shown above, we conclude that the 2D adaptive partitioning algorithm works. In the next section, some impulse responses of the 3D wavefield extrapolator are shown.

IMPULSE RESPONSE TESTS USING 3D GABOR EXTRAPOLATOR

The impulse response results in a homogeneous medium shows the in-progress research on the 3D Gabor extrapolation. The 3D data volume is set as 640 m by 640 m by 256 ms ($x \times y \times t$). The point source is located in the the center of the volume. One wave propagation is modelled. Numerical modeling of a 3D impulse response in a data volume ($x \times y \times t$) is done in this way: a point source (impulse) is convolved with a certain wavelet (Ormsby in this application) to create a seismic trace; the trace is then inserted into the 3D data volume (vertical coordinate in time) at the central position ($x_0 = x/2, y_0 = y/2$) (see Figure 6 (a)). The Gabor extrapolator is used to drive the impulse, resulting in a hyperboloidal-shape arrival in the data volume with apex right below the source point. A vertical section is plotted in the x direction through the source plane (Figure 6 (b)). A hyperbola shows arrival times in this vertical plane as those seen in a usual 2D shot record. If the vertical section moves away from the source plane, hyperbolic arrival times still show up; however, the arrivals are later than those in the source plane (compare Figure 6 (b) and (c)). Created are also time slices to show the patterns in the planes perpendicular to the vertical sections. As time moves away from the apex to later time, circular rings are seen corresponding to arrival times in horizontal planes. The later the time is, the larger the circles are (compare Figure 6 (d) to (e)).

A 3D view of the impulse response is shown in Figure 6 (f) as a cone-shaped surface of arrivals.

CONCLUSION

The adaptive partitioning with lateral position error extends easily from 1D to 2D as required for 3D Gabor imaging. The 2D adaptive partitioning algorithm has been coded into Matlab programs. The partitioning software can generate partitions on the velocity structure whose complexity compares to that, which may be used in Gabor depth imaging. The impulse response test shows initial functionality in 3D. 3D Gabor imaging test will be conducted in the near future.

ACKNOWLEDGMENTS

We wish to thank the Consortium of Research in Elastic Wave Exploration Seismology (CREWES) and the sponsors for financial support of this research. Thanks goes to the Pacific Institute of Mathematical Sciences (PIMS), Mathematics of Information Technology and Complex Systems (MITACS) and the Pseudodifferential Operator Theory in Seismic Imaging (POTSI) for financial supports. We thank Chad Hogan and David Henley for their careful reviewing of this paper and giving constructive suggestions.

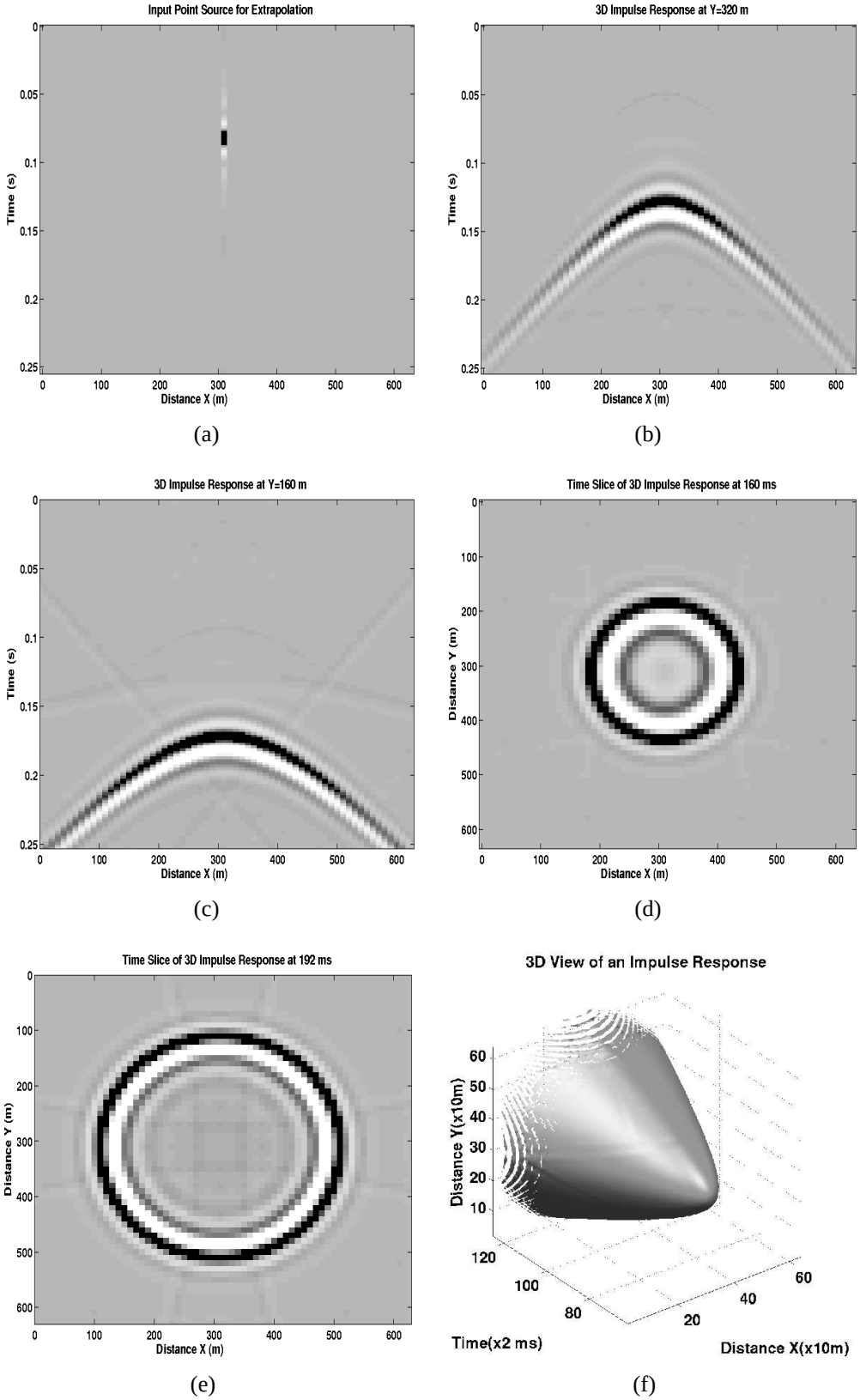

FIG. 6. 3D impulse response test for the Gabor imaging. (a) Before extrapolation. (b) After extrapolation (in the center). (c) After extrapolation(away from the center). (d) Time slice at 160 ms. (e) Time slice at 192 ms. (f) 3D view of the impulse response.

REFERENCES

Ferguson, R. J., and Margrave, G. F., 2002, Prestack depth migration by symmetric nonstationary phase shift: Geophysics, **67**, No. 2, 594–603.

Grossman, J. P., Margrave, G. F., and Lamoureux, M. P., 2002, Fast wavefield extrapolation by phase-shift in the nonuniform Gabor domain: CREWES Research Report, **14**.

Ma, Y., and Margrave, G. F., 2005a, A new adaptive windowing algorithm for the Gabor depth imaging: CREWES Research Report, **17**.

Ma, Y., and Margrave, G. F., 2005b, Prestack depth migration with the Gabor transform: CREWES Research Report, **17**.

Ma, Y., and Margrave, G. F., 2006a, Gabor depth imaging using a new adaptive partitioning algorithm: CREWES Research Report, **18**.

Ma, Y., and Margrave, G. F., 2006b, Prestack depth imaging with the Gabor transform: SEG Expanded Abstracts, **25**, 2504–2508.

Margrave, G. F., Al-Saleh, S. M., Geiger, H. D., and Lamoureux, M. P., 2004, The FOCI algorithm for seismic depth migration: CREWES Research Report, **16**.

Margrave, G. F., and Ferguson, R. J., 1999, Wavefield extrapolation by nonstationary phase shift: Geophysics, **64**, No. 4, 1067–1078.

Margrave, G. F., Geiger, H. D., Al-Saleh, S. M., and Lamoureux, M. P., 2006, Improving explicit seismic depth migration with a stabilizing wiener filter and spatial resampling: Geophysics, **71**, No. 3, S111–S120.

Stoffa, P. L., Fokkema, J. T., de Luna Freire, R. M., and Kessinger, W. P., 1990, Split-step fourier migration: Geophysics, **55**, 410–421.